Electronic Supplementary Material (ESI) for Journal of Materials Chemistry A.

Novel inorganic fillers of 1D hydroxyapatite nanowires induced superior energy storage performances of P(VDF-HFP)-based composite films

Yu Cheng[1], Zhongbin Pan[1*], Hanxi Chen[1], Xiangping Ding[1], Zhicheng Li[1], Xu Fan[1], Jinjun Liu[1*], Peng Li[2], Jinhong Yu[3], and Jiwei Zhai[4*]

[1]School of Materials Science and Chemical Engineering, Ningbo University, Zhejiang, Ningbo 315211, China. Email: panzhongbin@163.com (Zhongbin Pan), liujinjun1@nbu.edu.cn (Jinjun Liu)

[2]School of Materials Science and Engineering, Liaocheng University, Liaocheng 252059, China.

[3]Key Laboratory of Marine Materials and Related Technologies, Zhejiang Key Laboratory of Marine Materials and Protective Technologies, Ningbo Institute of Materials, Technology and Engineering, Chinese Academy of Sciences, University of Chinese Academy of Sciences, Zhejiang, Ningbo 315201, China.

[4]School of Materials Science & Engineering, Tongji University, 4800 Caoan Road, Shanghai 201804, China. Email: apzhai@tongji.edu.cn (Jiwei Zhai)

Characterization

The cross-sectional views of the nanocomposites, characterization was carried out by using field emission scanning electron microscopy (FE-SEM) and transmission electron microscopy (TEM). The crystalline structure of the material was obtained by X-ray diffraction (XRD) on a D8 Advance X-ray diffractometer. The infrared spectrum was gained by Fourier-transform infrared spectroscopy. The dielectric performances of the nanocomposites were measured at room temperature by means of an LCR meter from 10^2 Hz to 10^6 Hz with 1000 mV. The *D*-*E* loops were measured with the Premier II ferroelectric test system (Poly *K*, United States). The Young's modulus values were derived from strain–stress curves measured with a TA RSA-G2 Solids Analyzer, using a constant linear stretching rate of 10 mm/min.

Finite Element Simulations of Dielectric Breakdown

For further confirm the effect of the nonequilibrium structure on the dielectric breakdown strength of the composite films, the potential distributions, electric field and the electric tree channels were simulated via MATLAB and COMSOL Multiphysics. The progression chance *p* of electric tree divergence is defined in the percolation model as well as the fractal media decomposition model as follows

$$p(i',j' - i,j) = \frac{(\phi_{i',j'} - \phi_{i,j} - \phi_{P(VDF-HFP)})^{\eta}}{\sum(\phi_{i',j'} - \phi_{i,j} - \phi_{P(VDF-HFP)})^{\eta}} + (\phi_{i',j'} - \phi_{i'',j''} - \phi_{P(VDF-HFP)})^{\eta} - loss$$

where $\phi_{P(VDF-HFP)}$, $\phi_{i,j}$, $\phi_{i',j'}$, η and $\phi_{i'',j''}$ were the threshold electrical potential of the neat P(VDF-HFP), electrical potential of discharged point, probable point, fractal dimension and linked point, respectively. The *loss* represented evolve loss of tip electric tree channels.

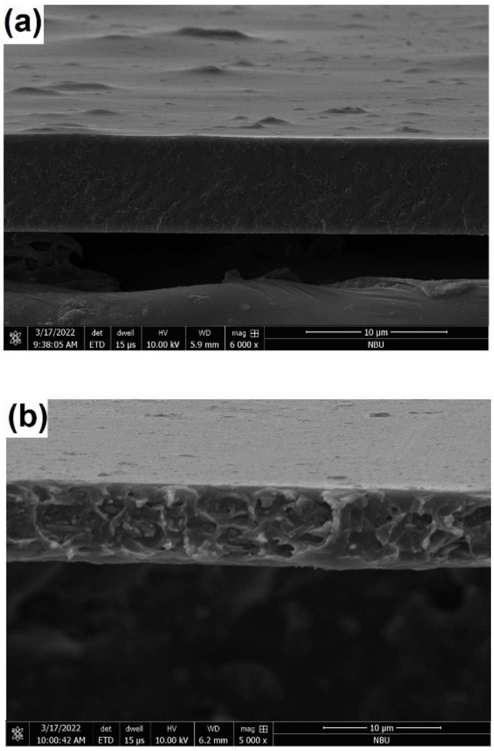

Fig. S1. (a) Cross-sectional SEM images of P(VDF-HFP) film; (b) Cross-sectional SEM images of P(VDF-HFP)/HAP NWs-4 nanocomposite film.

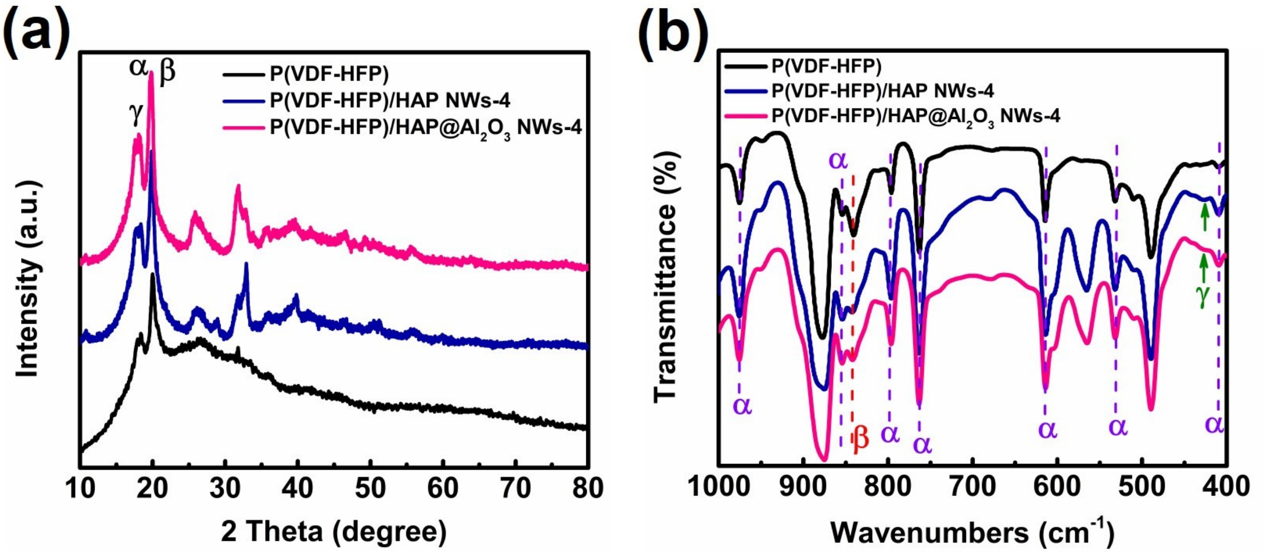

Fig. S2. (a) XRD patterns, (b) FT-IR spectra of P(VDF-HFP), P(VDF-HFP)/HAP NWs-4 and P(VDF-HFP)/HAP@Al$_2$O$_3$ NWs-4.

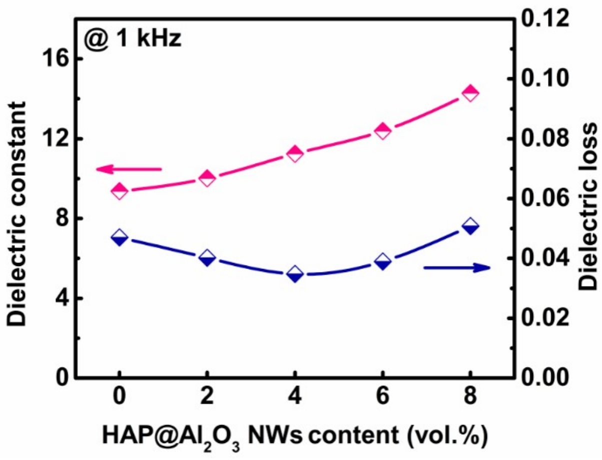

Fig. S3. Dielectric constant and dielectric loss with frequency of the P(VDF-HFP) and P(VDF-HFP)/HAP@Al$_2$O$_3$ NWs nanocomposites as a function of HAP@Al$_2$O$_3$ NWs contents.

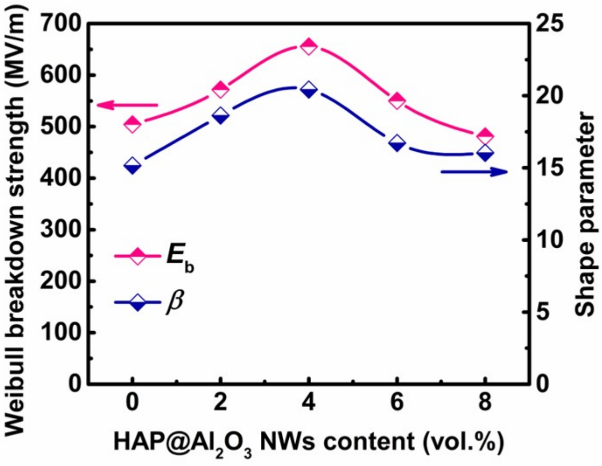

Fig. S4. Characteristic breakdown strength (E_b) and shape parameter (β) of the P(VDF-HFP) and P(VDF-HFP)/HAP@Al_2O_3 NWs nanocomposites as a function of HAP@Al_2O_3 NWs contents.

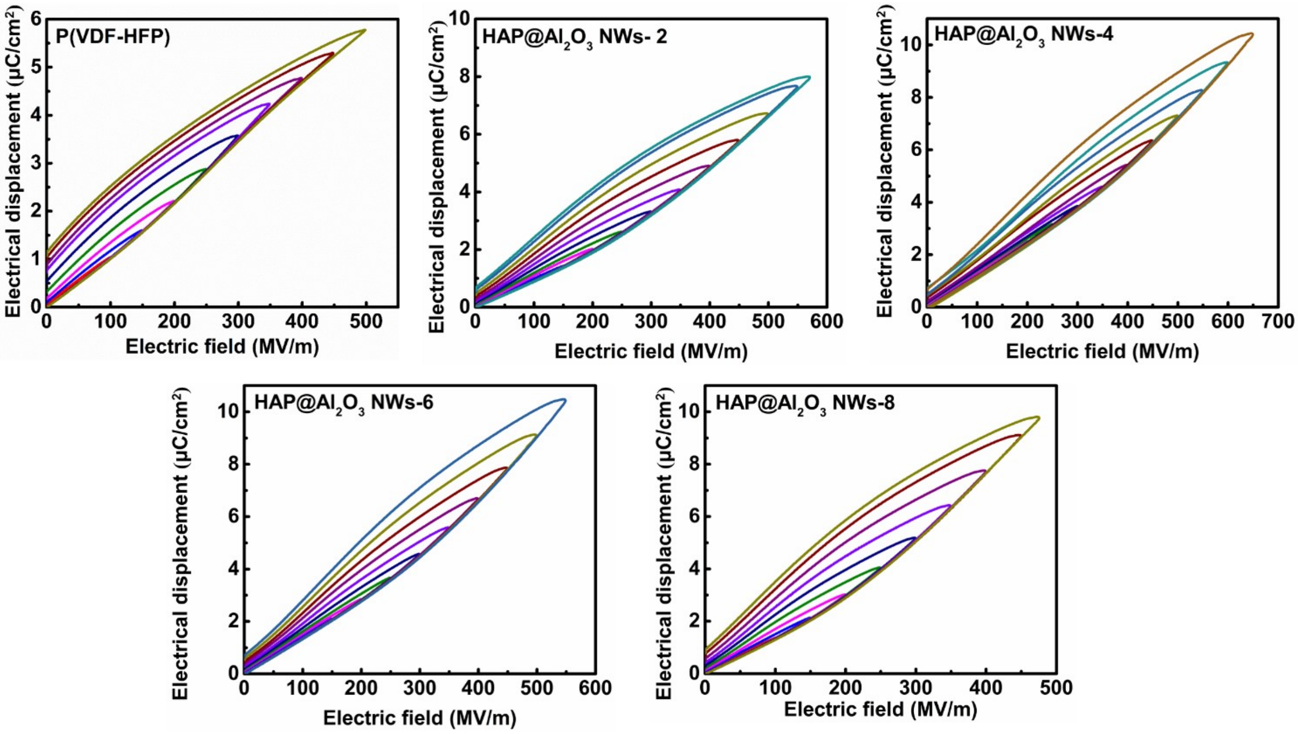

Fig. S5. *D*−*E* curves of the nanocomposites of the P(VDF-HFP) and P(VDF-HFP)/HAP@Al_2O_3 NWs nanocomposites as a function of HAP@Al_2O_3 NWs contents.

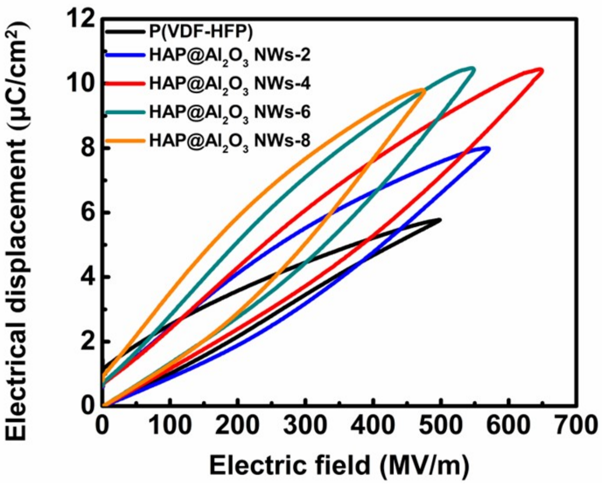

Fig. S6. *D*−*E* curves of the pristine P(VDF-HFP) and P(VDF-HFP)/HAP@Al$_2$O$_3$ NWs nanocomposites as a function of HAP@Al$_2$O$_3$ NWs contents at the highest electric field.

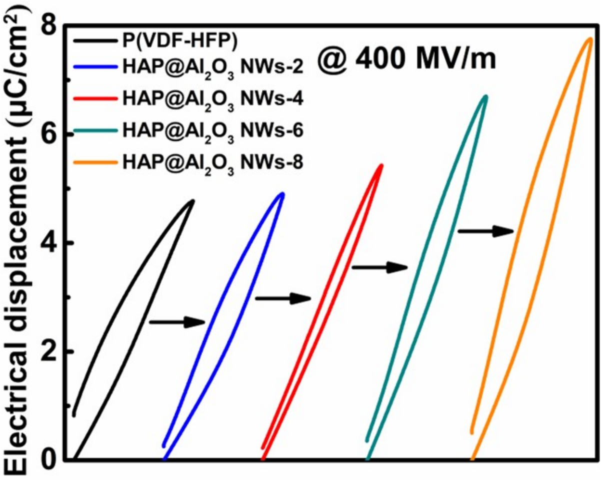

Fig. S7. The representative *D*–*E* loops of P(VDF-HFP) and P(VDF-HFP)/HAP@Al_2O_3 NWs nanocomposites as a function of HAP@Al_2O_3 NWs contents at 400 MV/m.

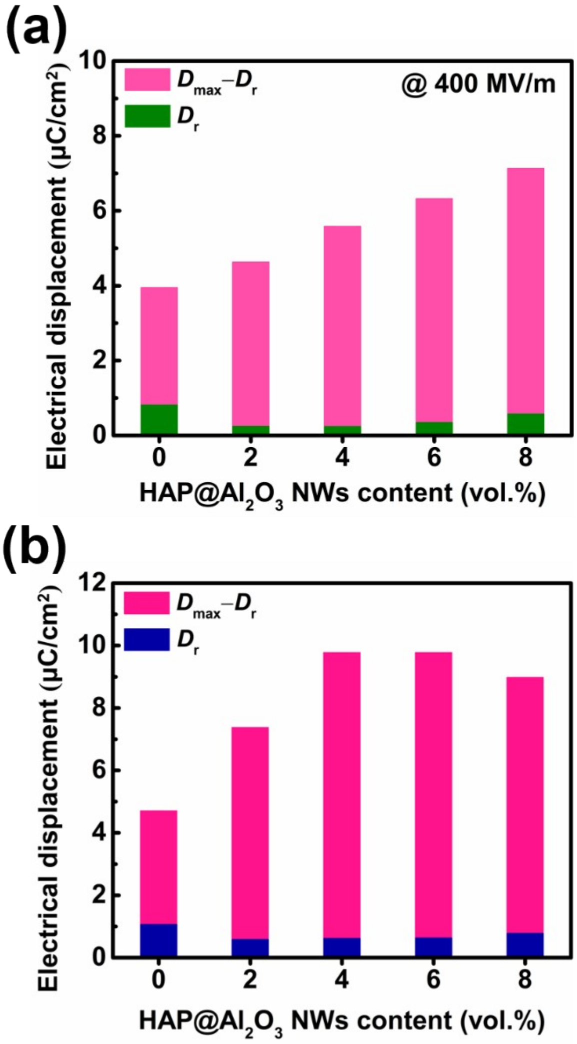

Fig. S8. (a) $D_{\mathrm{max}} - D_{\mathrm{r}}$ and D_{r} at 400 MV/m, (b) $D_{\mathrm{max}} - D_{\mathrm{r}}$ and D_{r} at the highest electric field of P(VDF-HFP) and P(VDF-HFP)/HAP@Al_2O_3 NWs nanocomposites as a function of HAP@Al_2O_3 NWs contents.

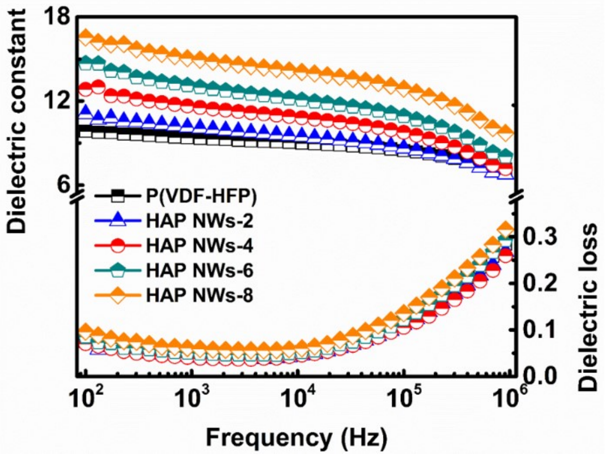

Fig. S9. Dielectric constant and dielectric loss with frequency of the pristine P(VDF-HFP) and P(VDF-HFP)/HAP NWs nanocomposites.

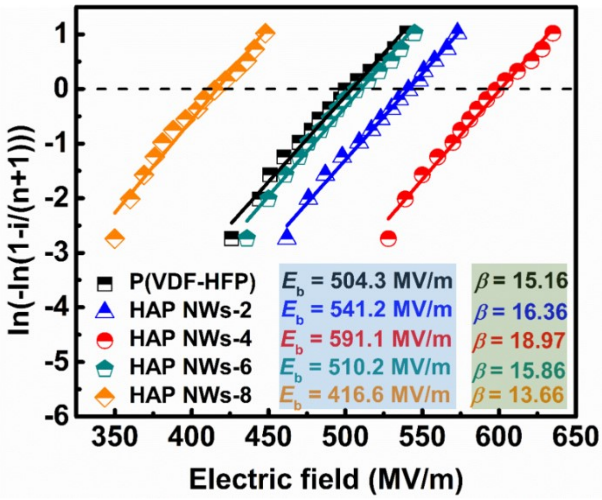

Fig. S10. Weibull plots and determined characteristic breakdown strength of the pristine P(VDF-HFP) and P(VDF-HFP)/HAP NWs nanocomposites.

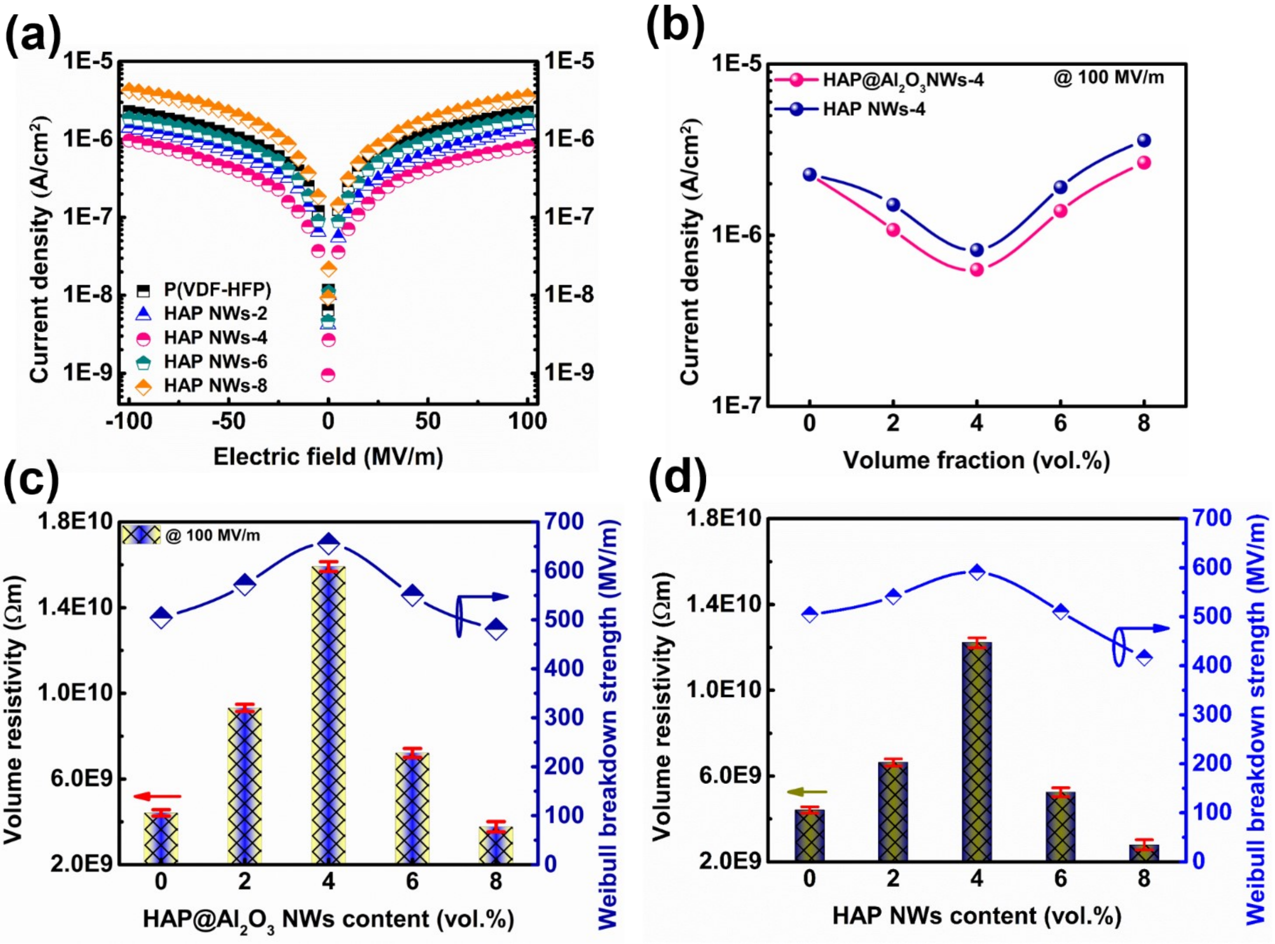

Fig. S11. (a) Leakage current densities as a function of electric field of the pristine P(VDF-HFP) and P(VDF-HFP)/HAP NWs nanocomposites; (b) Leakage current densities as a function of nanocomposites loaded with the different contents of HAP NWs and HAP@Al_2O_3 NWs; c) Volume resistivity as a function of nanocomposites loaded with the different contents HAP@Al_2O_3 NWs; d) Volume resistivity as a function of nanocomposites loaded with the different contents HAP NWs.

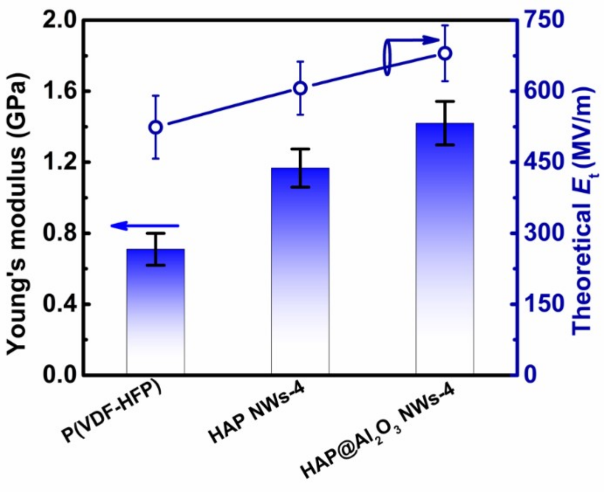

Fig. S12. Young's modulus and theoretical breakdown strength of pure P(VDF-HFP), 4vol% P(VDF-HFP)/HAP NWs, and 4vol% P(VDF-HFP)/HAP@Al_2O_3 NWs.

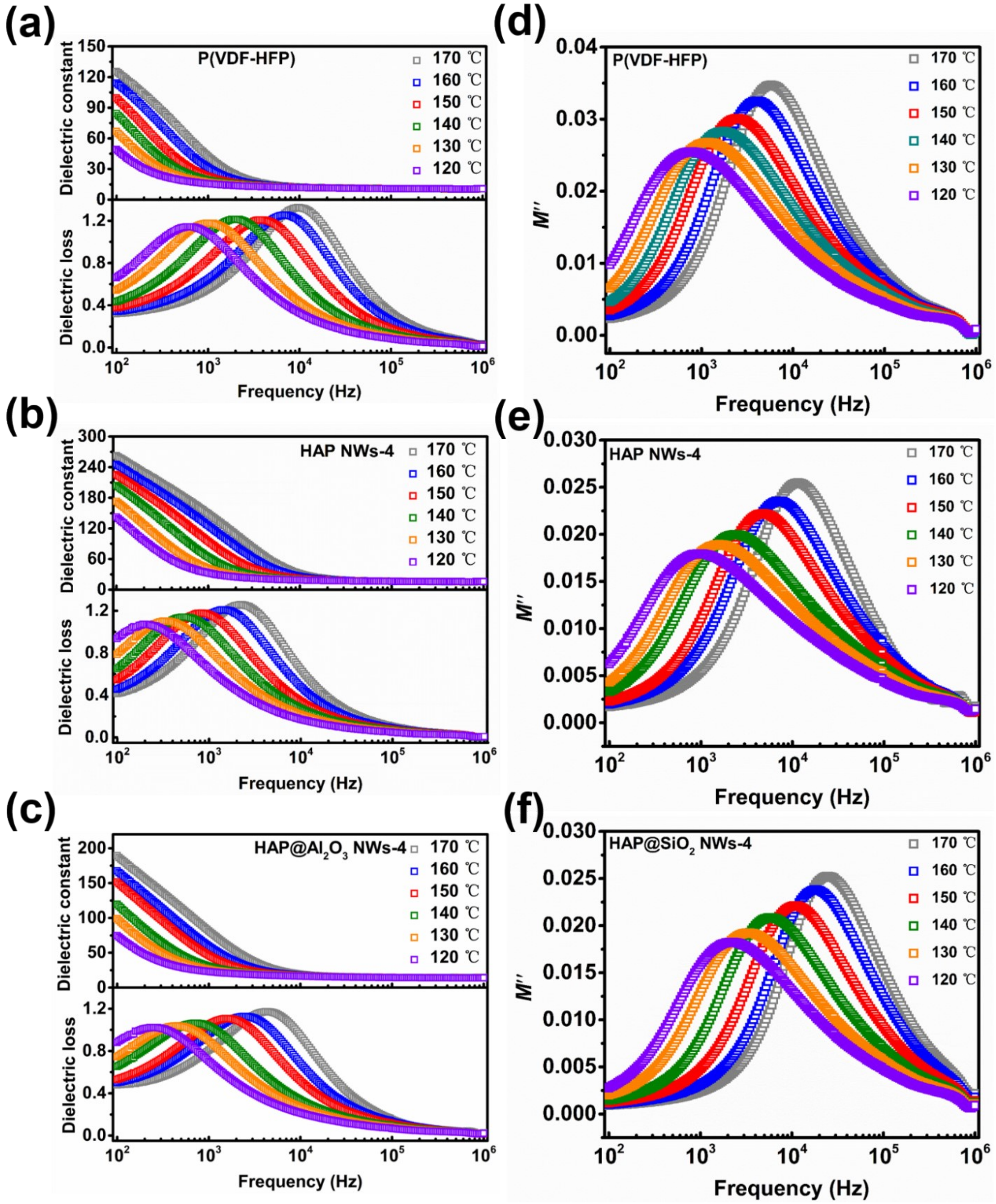

Fig. S13. Broadband dielectric for composite dielectrics at different temperatures of (a) pristine P(VDF-HFP), (b) 4 vol% P(VDF-HFP)/HAP NWs, and (c) 4 vol% P(VDF-HFP)/HAP@Al_2O_3 NWs; Frequency-dependence of imaginary electric modulus (*M″*) for (d) the pristine P(VDF-HFP), (e) 4 vol% P(VDF-HFP)/HAP NWs, and (f) 4 vol% P(VDF-HFP)/HAP@Al_2O_3 NWs composite films.

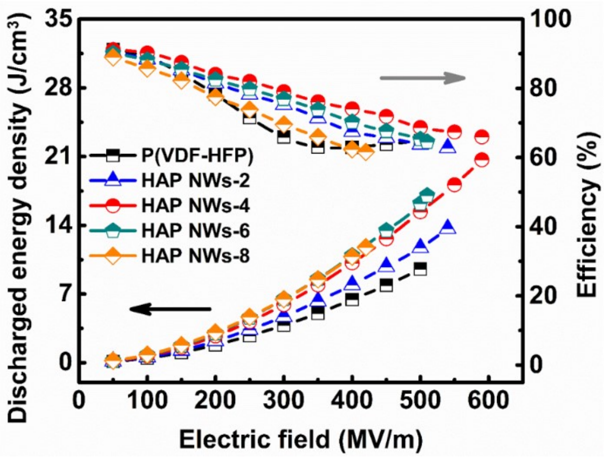

Fig. S14. Discharged energy density and efficiency of the pristine P(VDF-HFP) and P(VDF-HFP)/HAP NWs nanocomposites.

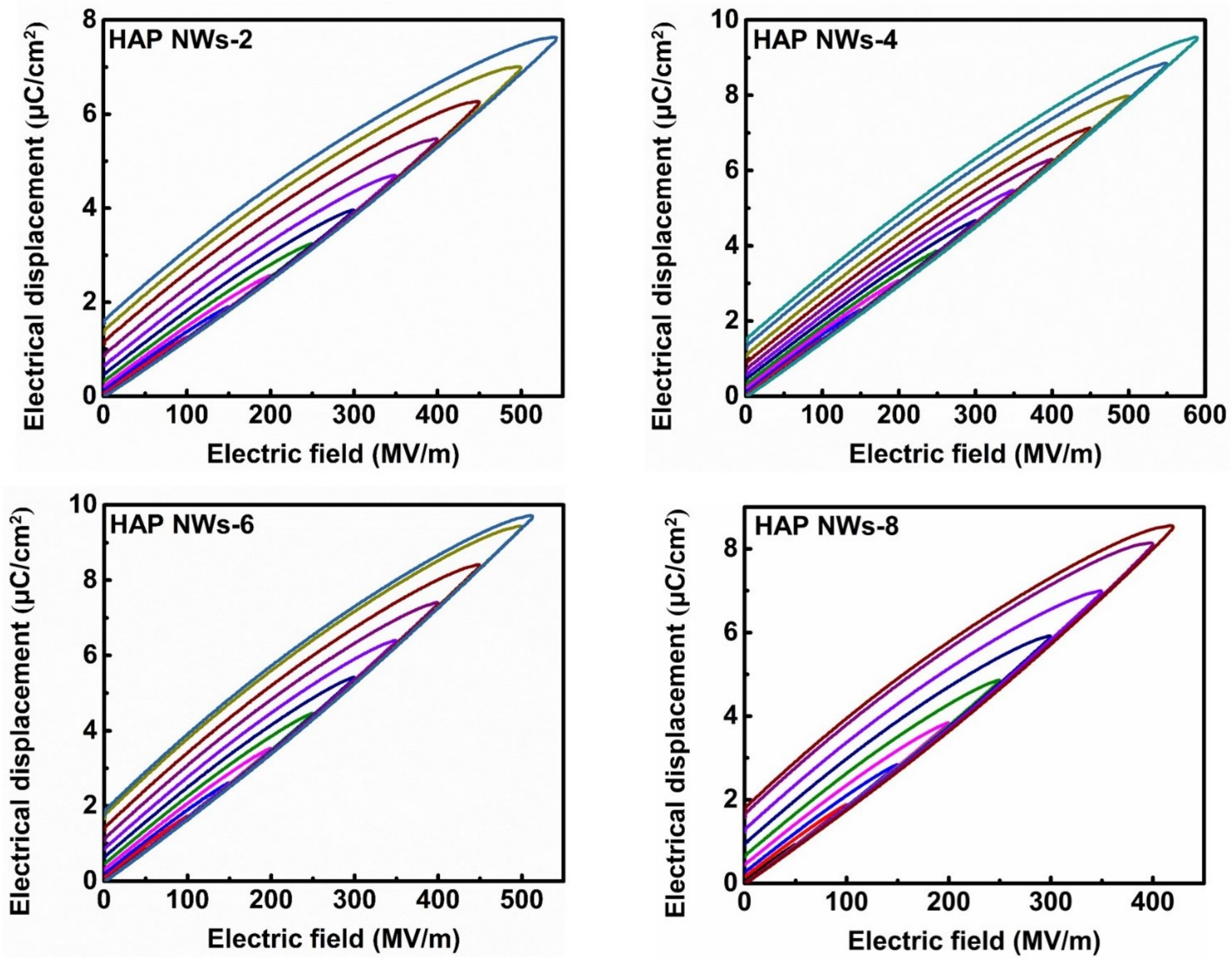

Fig. S15. The *D*−*E* curves of P(VDF-HFP)/HAP NWs nanocomposites as a function of HAP NWs contents.

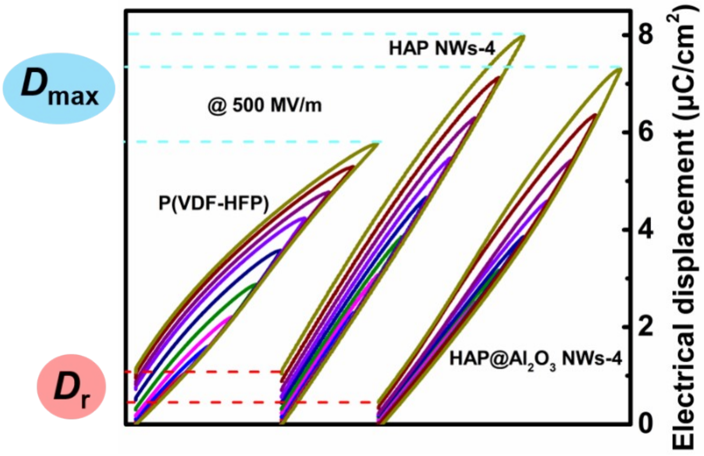

Fig. S16. The *D*−*E* loops of P(VDF-HFP), P(VDF-HFP)/HAP NWs-4 and P(VDF-HFP)/HAP@Al$_2$O$_3$ NWs-4 nanocomposites at 500 MV/m.

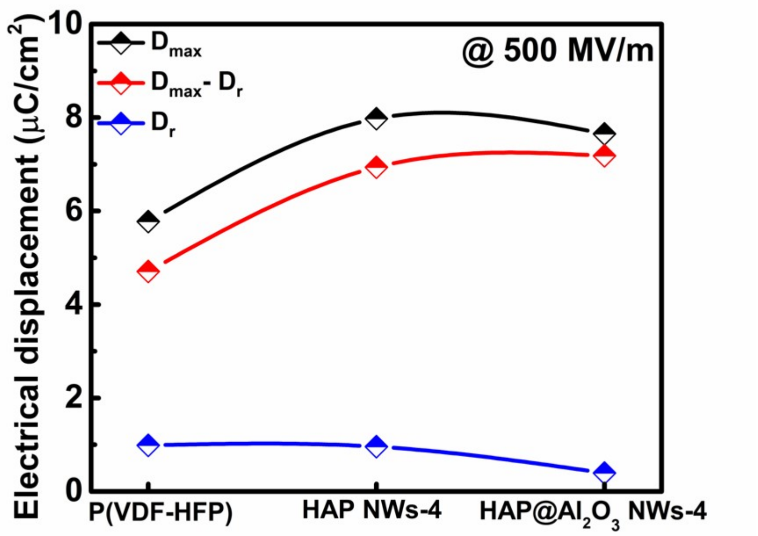

Figure S17. The $D_{\max}$, $D_{\max}-D_{\mathrm{r}}$ and D_{r} of P(VDF-HFP), P(VDF-HFP)/HAP NWs-4 and P(VDF-HFP)/HAP@Al_2O_3 NWs-4 nanocomposites at 500 MV/m.